

Phase-Field Models for Eutectic Solidification

Daniel Lewis, Tamás Pusztai, László Gránásy, James Warren, and William Boettinger

This article discusses two methods for modeling eutectic solidification using the phase-field approach. First, a multi-phase-field model is used to study the three-dimensional morphological evolution of binary eutectics. Performing the calculations in three dimensions allows observation of both lamellar and rod-like structures as well as transient phenomena such as lamellar fault motion, rod-branching, and nucleation or elimination of phases as solidification progresses. The second approach models multiple eutectic grains where the crystallizing phases have an orientation relationship. This approach is promising for modeling complex solidification microstructures.

INTRODUCTION

The sharp interface approach to the modeling of eutectic solidification is illustrated in the widely referenced paper by Jackson and Hunt.¹ For eutectics growing at constant velocity, the model computes the undercooling below the eutectic temperature, averaged across the solid-liquid interface, for lamellar and rod geometries for a variety of spacings. For a constant interface velocity, the preferred geometry and spacing is that with the lowest average undercooling. This procedure determines a balance between solute transport, where small eutectic spacing is favored, and solid-liquid interface curvature during the solidification process, which favors a large eutectic spacing. This modeling approach does not deal with transients of the microstructure selection process or its three-dimensional (3-D) nature. In addition, many eutectics do not exhibit lamellar or rod structure because at least one solid phase has anisotropic growth kinetics. Such irregular binary, as well as many ternary,

eutectic microstructures are poorly understood. The phase-field technique described here provides materials scientists with a powerful methodology for studying these processes. This article outlines some of the progress being made toward applying phase field methods to eutectic solidification.

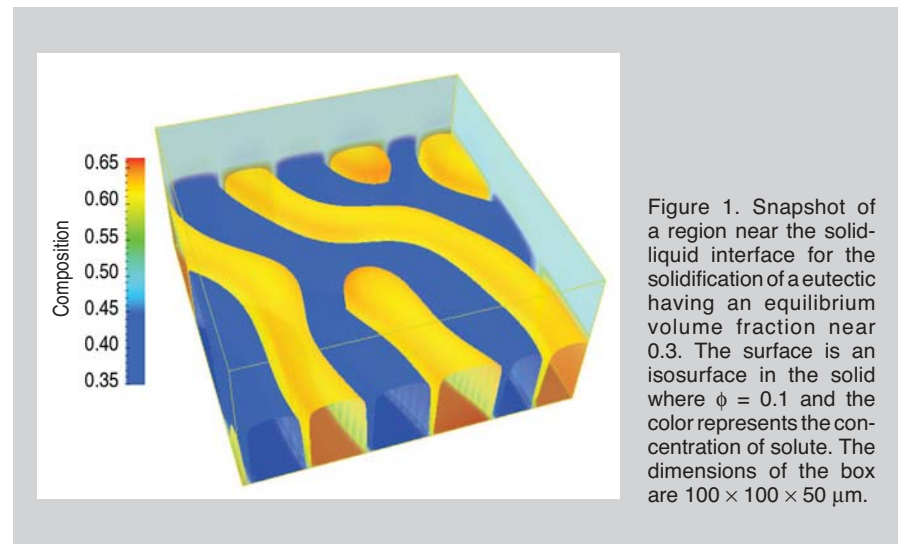
The materials science implementation of the phase-field technique (for example, see References 2–12) is based on prior work treating solid state transformations in spinodal alloys¹³ and in order-disorder alloys.¹⁴ Unlike other models of microstructure development, interfaces in the phase-field formulation are not considered infinitely thin or sharp, but are considered to be diffuse and have finite thickness. One advantage of diffuse interface models is that explicit mathematical boundary tracking of the interface position is no longer necessary. This is important because in the sharp interface approach, boundary conditions must be applied at the moving boundary to conserve mass and heat and to set the appropriate thermodynamic/attachment kinetic conditions. The phase-field

method can easily handle time-dependent growth geometries caused by nucleation, coalescence, or elimination of phase particles. Numerical solution methods for the phase-field differential equations can be straightforward but computationally intense.

Early phase field models typically treated single-phase cellular and dendritic growth from the liquid. Phase-field models of eutectic solidification are more challenging to construct due to the presence of multiple solid phases. A model of binary eutectic solidification, for example, must describe the transformation of a single-phase liquid to two solid phases having different concentrations. In addition to eutectic transformations, the multi-phase-field method has been applied to monotectic and peritectic transformations.^{7,15}

MULTI-PHASE-FIELD DIRECTIONAL SOLIDIFICATION MODEL

Binary rod-like and lamellar morphologies can be computed using the multi-phase-field method. This method



is a natural formulation that combines free-energy expressions for each phase into a single free-energy expression for the system. Simple eutectic systems can be constructed from three ideal solution models that form a pair of intersecting lens-shaped diagrams. The model presented in this work is adapted from the model for a binary alloy presented by Nestler et al.⁷

In a manner similar to that of Steinbach et al.⁴ or Wheeler et al.,⁵ the multi-phase-field order parameter ϕ_α is introduced for each phase α . This parameter ranges from $\phi_\alpha = 1$ in bulk α to $\phi_\alpha = 0$ in regions that are not bulk α . In an n phase system, the sum of all ϕ at every point in space obeys the constraint shown in Table I, Equation 1. (All equations are listed in Table I).

The multi-phase-field free energy functional has the form shown in Equation 2.

In a two-phase system, the gradient energy terms in Equation 2 reduce to the expression for a single-order parameter model.¹¹ The bulk free energy is given in Equation 3.

G_α is an ideal solution model (enthalpy of mixing is equal to zero) for phase α . The interpolating functions, p , are given in Equation 4.

Note that $p(1) = 1$ and $p'(1) = 0$, while $p(0) = 0$ and $p'(0) = 0$. To get linear scaling of the liquid-solid surface energy of the pure components at fixed interface thickness, ϵ^2 and W are linearly scaled with temperature (see Equation 5).

$\Delta S_i^{\alpha \rightarrow \beta}$ is the entropy of transformation from phase α to phase β and $\Delta c_{\alpha\beta}$ is the interface thickness between phases α and β . $\dot{\phi}_\alpha$ and \dot{c} may be computed using the simplest¹⁶ forms for the equations of motion. The equation of motion for phase α is Equation 6.

M_ϕ is proportional to the interface attachment kinetics for phase α . For an m component system, the equation of motion for component i is shown in Equation 7.

M_c is a function that adjusts the solute diffusivity depending on the local value of the phase field. The terms $\delta F/\delta c$ and $\delta F/\delta \phi$ are the variational derivatives of c and ϕ , respectively.

Two-dimensional simulations were completed for comparison to previously published work.⁷ After satisfactory results were obtained, the equations

were extended to three dimensions. The 3-D equations were solved using a finite difference scheme in a computational volume with $100 \times 100 \times 50$ grid points representing $10 \times 10 \times 5 \mu\text{m}^3$. The short axis of the computational volume is parallel to the solidification direction. This choice allows the study of the morphological changes at the solid-liquid interface without a large computational array. To specify the initial

conditions, the computational volume was split in half. Relative to the solidification direction, the top half was filled with liquid at the eutectic composition and the bottom half was filled with a random solid mixture.

In order to simulate directional solidification, the equations of motion were transformed into a moving reference frame. A fixed temperature gradient was imposed on the computational

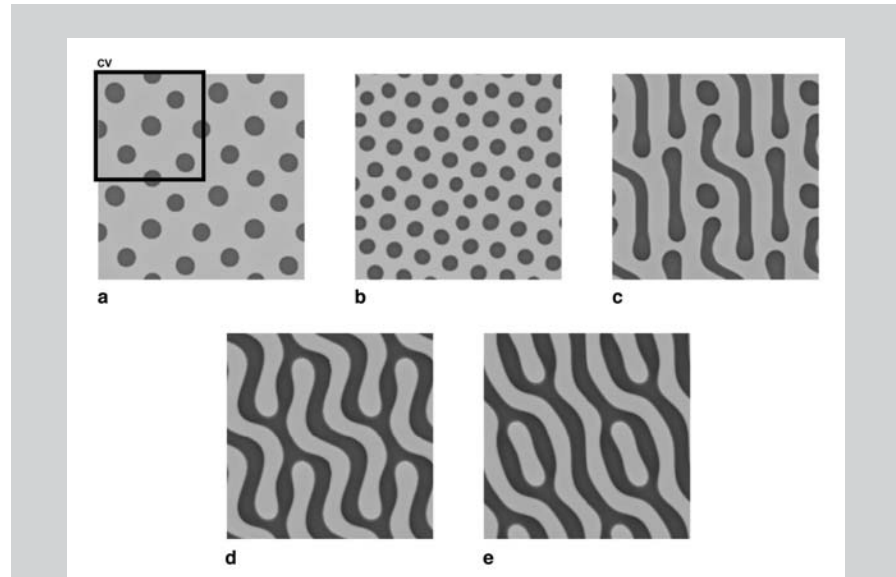


Figure 2. Simulation results for different minor phase volume fractions approaching steady-state solidification. The minor phase volume fractions are (a) 0.178, (b) 0.305, (c) 0.379, (d) 0.485, and (e) 0.499. Each image represents a 2×2 tiling of the computation volume ($200 \times 200 \mu\text{m}$) perpendicular to the solidification direction. The computational volume (CV) is indicated by the box in pane (a). As the volume fraction of the minor phase increases from (a) to (e), a lamellar arrangement of phases becomes more prominent.

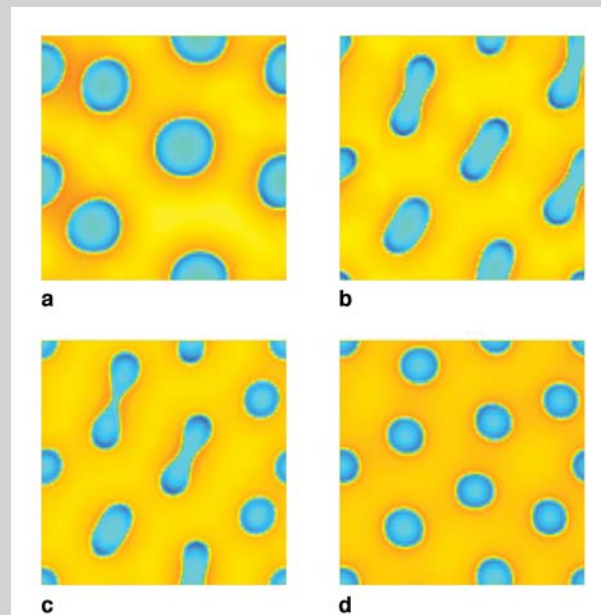


Figure 3. A sequence of images showing different stages of the rod-branching process. This simulation uses a solute diffusivity 100 times smaller than the previous simulation where the minor phase volume fraction is 0.178 (Figure 2a). Each image represents $100 \times 100 \mu\text{m}$.

Table I. Equations

$$\sum_{\alpha=1}^n \phi_{\alpha} = 1 \quad (1)$$

$$F(c, \phi_{\alpha}, \nabla \phi_{\alpha}) = \int \left\{ f_{\text{bulk}} + \sum_{\alpha, \beta} \frac{1}{4} \varepsilon_{\alpha\beta}^2 (\phi_{\alpha} \nabla \phi_{\beta} - \phi_{\beta} \nabla \phi_{\alpha})^2 \right\} dV \quad (2)$$

$$f_{\text{bulk}} = \sum_{\alpha} G_{\alpha} p(\phi_{\alpha}) + \sum_{\alpha, \beta=1}^n \frac{1}{8} W_{\alpha, \beta} \phi_{\alpha}^2 \phi_{\beta}^2 \quad (3)$$

$$p(\phi_{\alpha}) = \phi_{\alpha}^3 (6\phi_{\alpha}^2 - 15\phi_{\alpha} + 10) \quad (4)$$

$$\begin{aligned} \varepsilon_{\alpha, \beta}^2 &\propto \Delta S_i^{\alpha \rightarrow \beta} T \Delta_{\alpha\beta} \\ W_{\alpha\beta} &\propto \Delta S_i^{\alpha \rightarrow \beta} T \Delta_{\alpha\beta} \end{aligned} \quad (5)$$

$$\dot{\phi}_{\alpha} = -M_{\phi_{\alpha}} \frac{\delta F}{\delta \phi_{\alpha}} \quad (6)$$

$$\dot{c}_i = \nabla \cdot \left(M_{c_i} (c_1 c_2 \dots c_m) \nabla \frac{\delta F}{\delta c_i} \right) \quad (7)$$

$$F = \int \left\{ \frac{1}{2} \varepsilon_{\phi}^2 T \Gamma^2 (\nabla \phi, \dots) + \frac{1}{2} \varepsilon_c^2 T (\nabla c)^2 + f_{\text{bulk}} + f_{\text{orient}} \right\} dV \quad (8)$$

$$f_{\text{bulk}} = \frac{1}{4} \left[(1-c) W_A + c W_B \right] T \phi^2 (1-\phi^2) + [1-p(\phi)] f_{\text{solid}} + p(\phi) f_{\text{liquid}} \quad (9)$$

$$f_{\text{orient}} = [1-p(\phi)] M F(\nabla \theta) \quad (10)$$

$$\begin{aligned} \frac{\partial \phi}{\partial t} &= [(1-c)m_A + cm_B] \varepsilon_{\phi}^2 \left[\tilde{\nabla} \cdot (s^2 \tilde{\nabla} \phi) - \frac{\partial}{\partial \bar{x}} \left(s s' \frac{\partial \phi}{\partial \bar{y}} \right) + \frac{\partial}{\partial \bar{y}} \left(s s' \frac{\partial \phi}{\partial \bar{x}} \right) \right] \\ &+ [(1-c)m_A + cm_B] [(1-c)Q_A + cQ_B + Q] \end{aligned} \quad (11)$$

$$Q_{A,B} = -\frac{\xi^2}{\delta_{A,B}^2} g'(\phi) + \frac{\xi^2 L_{A,B} (T - T_{A,B})}{6\sqrt{2} \gamma_{A,B} \delta_{A,B} T} p'(\phi) \quad (12)$$

$$Q = \frac{\xi^2 T_A [M F(l \tilde{\nabla} \theta) \xi^{-1} - \Delta \Omega c (1-c)]}{6\sqrt{2} \gamma_A \delta_A T} p'(\phi) \quad (13)$$

$$\frac{\partial c}{\partial t} = \tilde{\nabla} \cdot \left\{ \begin{aligned} &\lambda \left[1 - c(1-c) \frac{v}{RT} 2[p(\phi) \Delta \Omega + \Omega_s] \right] \tilde{\nabla} c \\ &+ \lambda c(1-c) \frac{v}{R} \left[\left(g' \delta W + p' \frac{\delta \Delta g + \Delta \Omega (1-2c)}{T} \right) \tilde{\nabla} \phi \right] \\ &- \tilde{\nabla} \zeta_c \frac{6\sqrt{2} \gamma_A \delta_A v}{\xi^2 RT_A} \tilde{\nabla}^2 c \end{aligned} \right\} \quad (14)$$

$$\frac{\partial \theta}{\partial t} = \xi \chi M \tilde{\nabla} \cdot \left\{ (1-p) F'(l \nabla \theta) \frac{\tilde{\nabla} \theta}{| \tilde{\nabla} \theta |} \right\} \quad (15)$$

$$\begin{aligned} h(c) &= \frac{1}{2} \left\{ 1 + \cos \{ (c - c_{\alpha}) / (c_{\beta} - c_{\alpha}) 2\pi \} \right\} \\ F_1(l \nabla \theta) &= | \nabla \theta | \\ F_2(l \nabla \theta) &= a + b | \cos(2m\pi d | \nabla \theta | + \psi) | \end{aligned} \quad (16)$$

volume in the solidification direction. No attempt was made to study the effect of the temperature gradient on the eutectic morphology. Material was advected into the computational volume in the liquid phase at the eutectic composition. Solid was then advected out of the computational volume after the eutectic transformation. The boundary conditions on the remaining faces of the computational volume were periodic.

Five simulations were completed, each with different equilibrium volume fractions of the solid phases. This was accomplished by reducing the equilibrium melting temperature for one of the solid phases. The liquid and solid diffusion coefficients were set to 1×10^{-8} m²/s; for the pure materials, the interface thickness was on the order of 1 μ m and the surface energy on the order of 1×10^{-5} J/m². The solidification velocity was 7 mm/s.

The choice of solid diffusivity produced rapid changes in the solid-phase connectivity as the microstructure evolved toward steady state. With a more realistic solid-state diffusivity, the morphology changes to produce a similar steady-state microstructure would require longer simulation times. In a simple eutectic system such as tin-lead, the lamellar spacing is approximately 5 μ m for a solidification velocity of 1 μ m/s.¹⁷ Interface thicknesses are thought to be on the order of a few atomic distances. The choice of interface thickness for the simulations is related to the resolution of the grid used for the numerical computation. More realistic interface thicknesses require an increased grid resolution and therefore extend computation times.

The average solid-liquid interface temperature was computed and calculations were run until the increase in average interface temperature (decrease in undercooling) was no more than 0.001 K over a solidification distance of approximately 0.2 μ m. This was the definition of steady state in this study. This rate of temperature change does not guarantee that the structure obtained is one of minimum undercooling. The eutectic morphology obtained could be a metastable morphology or a morphology approaching a minimum undercooling at a very slow rate.

POLYCRYSTALLINE EUTECTIC SOLIDIFICATION MODEL

Figure 1 shows the steady-state solidification microstructure near the solid-liquid interface for an equilibrium volume fraction of 0.5. This image shows the volume used to perform the computation. The depicted surface is an isosurface in the solid phase fields where $\phi_i = 0.1$. Mapped onto this surface is the concentration field. Figure 2a through 2e shows simulation results for minor phase volume fractions of 0.178, 0.305, 0.379, 0.485, and 0.499, respectively. Each of these images show a similar isosurface located near the solid-liquid interface onto which the concentration field has been mapped. The shading indicates the solute concentration where the light phase is solute poor and the dark phase is solute rich. The images show the solid-liquid interface oriented perpendicular to the growth direction (transverse) and represent a periodic tiling of the computational volume repeated two times along each axis. The projection of the computational volume is indicated by the outline in Figure 2a. Each of the rods in Figure 2a and 2b is approximately a cylinder of circular cross section and is disconnected from other rod-like phases in the transverse direction. The remaining images show structures that contain lamellae at volume fractions closer to 0.5.

For the system with a minor phase volume fraction of 0.178, a second simulation was performed. Starting from the same initial conditions, the solid phase diffusion coefficients were reduced by a factor of 100 and the microstructural evolution was observed. Figure 3a through 3d shows intermediate states from that simulation. Figure 3a shows a coarse rod structure, similar to transient states seen during the evolution of the simulation results presented in Figure 2a. Figure 3b and 3c shows the coarse rods in Figure 3a as they begin to elongate and ultimately split into two individual rods. Finally, Figure 3d shows the reduced average interphase spacing due to the decrease of the solid-state diffusivities. Although new rods may nucleate to decrease the average inter-rod spacing, existing rods may also undergo a branching process. An example of this spacing selection mechanism in the copper-chromium system has been reported previously.¹⁸

The described treatment enabled the simulation of multiple phases during eutectic solidification, but did not allow for differing crystallographic orientations in each of the solid phases. To allow for such an effect, the authors modified the phase-field model by Gránásy et al.^{19–21} developed for dendritic polycrystalline solidification, which itself extended work by Kobayashi et al.^{10,22} (See also Reference 11.)

In order to understand how this model treats orientation relationships between phases, a regular solution model is introduced, which is sufficient to describe eutectic growth when the crystal structure of the solids is the same, and couples it to an orientation parameter. The model of Gránásy is then modified to couple certain preferred orientations across the phase boundaries, for a more complete picture. Finally, a representative simulation of the equations in two dimensions is presented.

The model of Gránásy et al. treats the existence of grains with different crystallographic orientations by incorporating a non-conserved orientation field, $0 \leq \theta \leq 1$, that determines crystal orientation in the laboratory frame. In addition, the orientation is also specified in the liquid, where it is random and fluctuates in time at the finest resolution for a given simulation. While this may at first seem strange, this orientation field fluctuation is based on the observation that it is possible to have temporary short range order in simple liquids. This short range order is based on geometric constraints arising from mutual repulsion of atomic nuclei and on attractive interactions between the liquid atoms. Structural analysis of simulated liquid configurations, using Voronoi polyhedra or angular correlations, indicates the existence of face-centered cubic (fcc), hexagonal close packed, body-centered cubic, and icosahedral local atomic arrangements.^{23,24} Once these localized atomic structures are recognized, they temporarily specify a local orientation in the laboratory frame.

Additionally, to properly account for

the nucleation of grains in an undercooled melt, computer simulations and real-time experiments on colloidal suspensions²⁵ indicate that during nucleation these crystal-like clusters dynamically form and decay, and then reform again with different orientation, etc. To model this phenomenon, fluctuations of the structural and orientation order parameters (Langevin noise in the dynamic equations) are introduced, and a strong coupling between the two fields is prescribed.

As soon as the crystalline atomic order forms, it defines the orientation of the grain. (In complex liquids of low-symmetry molecules, the interpretation of this single orientation field is more straightforward; it can be viewed as a coarse-grained molecular orientation.)

The described ideas are implemented by adopting the free-energy functional shown in Equation 8, where ϵ_s and ϵ_c are constants and T the temperature. In this model, $\phi = 1$ in the bulk liquid and $\phi = 0$ in the solid. The function Γ contains information about the energy penalty for an interface and includes interface anisotropy. If the surface energy is isotropic, then $\Gamma = |\nabla\phi|$. For the anisotropic case considered here, $\Gamma = s(\zeta)|\nabla\phi|$, where ζ is the orientation of the crystal interface with respect to the local crystalline lattice. Thus $\zeta = \vartheta - 2\pi\theta/n$, where $\vartheta = \arctan[(\partial\phi/\partial y)/(\partial\phi/\partial x)]$ is the orientation of the interface normal with respect to the x-axis and n is the rotational symmetry of the crystal. In this case, $s(\zeta) = 1 + s_0 \cos[n\zeta]$, where s_0 is the magnitude of the anisotropy.

The bulk free energy has the form shown in Equation 9, where $W_{A,B}$ are related to the interface thickness and the surface energy of the pure materials,²⁶ $p(\phi)$, is defined by Equation 4, while f_{solid} and f_{liquid} are regular solution models. The orientation free energy has the form given in Equation 10. In previous treatments^{19,22} the function F was chosen by the prescription $F(\nabla\theta) = |\nabla\theta|$. This assigned an excess free energy to spatial changes of crystal orientation, thus preferring the formation of regions of uniform orientation or grains, while adding energy for grain boundaries. Due to the factor $[1 - p(\phi)]$, f_{orient} acts mostly in the solid. This relationship implies that the rotation of a nearest-neighbor

cluster in the disordered liquid will produce a small change in the liquid free energy, but rotation away from the predominant crystallographic orientation in the solid lattice will necessitate a substantial energetic penalty. A modified form of F is specified later in this article. Using reduced units of length, ξ , and time ξ^2/D_1 (where D_1 is the solute diffusivity in the liquid), the dimensionless equation of motion for the non-conserved phase field, ϕ , is shown in Equations 11–13.

Here, m_i , L_i , T_i , δ_i , and γ_i are the reduced mobility, the heat of fusion, the melting point, the interface thickness, and the interface free energy for the pure components $i = A$ and B . $\Delta\Omega = \Omega_L - \Omega_S$ is the difference between the volumetric interaction coefficients of the liquid and solid at temperature T . The quantities marked with tilde are dimensionless. Note that $\gamma_A \delta_A / T_A = \gamma_B \delta_B / T_B$ follows from the equilibrium conditions for the pure substances, unless temperature-dependent ϵ_θ or W_i are used (see treatment described previously). Equation 14 shows the time evolution of the chemical composition (a conserved

quantity), while Equation 15 shows the motion for the non-conserved orientation field, where $g' = \phi^3 - (3/2)\phi^2 + (1/2)\phi$ and $p' = 30\phi^2(1 - \phi)^2$, $\delta W = W_B - W_A$, $\delta\Delta g = \Delta g_B - \Delta g_A$, $\zeta_c = (\epsilon_c / \epsilon_\theta)^2$, λ and χ are the reduced diffusion coefficient and the reduced mobility of the orientational ordering, and R and v are the gas constant and the molar volume. To model thermal fluctuations, uncorrelated Gaussian noise is added to Equations 11 and 15 and a random diffusion current is added to Equation 14.

Setting $\epsilon_c = 0$ and $\Omega_L = \Omega_S = 0$, the model for describing primary dendritic solidification of ideal solutions (Gránásky et al.¹⁹) is recovered. This is next generalized to eutectic growth of two solid phases (α and β) of different chemical compositions and of different orientations.

For this study, several assumptions are made: First, in solids with a composition close to the equilibrium ones, the grain boundary model used for the single solid case is retained (i.e., $f_{\text{orient}} \propto |\nabla\theta|$). Second, at the interface between the two solid phases, a nonzero orientation change is preferred. This orientation

change is assumed to be independent of the inclination of the solid-solid interface. To implement these, the orientation free energy is assumed to be composition dependent: $f_{\text{orient}} = [1 - p(\phi)]MF(c, |\nabla\theta|)$, where $F = h(c)F_1(|\nabla\theta|) + [1 - h(c)]F_2(|\nabla\theta|) + 1/2 \epsilon_\theta^2 TM^{-1}|\nabla\theta|^2$. The gradient-squared term is needed to allow for grain boundary motion (besides grain rotation), as shown in Equation 16.^{10,27}

Here, c_α and c_β are the equilibrium solid compositions, a and b are constants, and d is the interface thickness. The control parameters m and ψ can both be used to define the preferred orientation change at the interface. Note that at intermediate compositions near solid-solid interfaces where $c_\alpha < c < c_\beta$, the function $h(c)$ approaches 0 and at equilibrium compositions where $c = c_\alpha$ or $c = c_\beta$ in the bulk solid, $h(c)$ approaches 1. Such intermediate compositions occur only at the $\alpha - \beta$ interface in the solid. Anisotropy of the interface free energy might be incorporated via making either ϵ_θ^2 or ψ dependent on the interface inclination angle $\vartheta_c = \arctan[(\partial c/\partial y)/(\partial c/\partial x)]$. While the functions used here have been chosen intuitively, for specific crystal structures, F_1 and F_2 can be deduced on physical grounds. Having defined these relationships, new terms emerge in the governing equations. The actual $F = h(c)F_1 + [1 - h(c)]F_2 + 1/2\epsilon_\theta^2 TM^{-1}|\nabla\theta|^2$ function enters into Equation 11, its first derivative $F' = h(c)F'_1 + [1 - h(c)]F'_2 + \epsilon_\theta^2 TM^{-1}|\nabla\theta|$ appears in Equation 15, and the terms shown below are introduced into the right hand side of Equation 14:

$$\tilde{\nabla}\lambda c(1-c) \frac{v}{RT} M \times$$

$$\left\{ \begin{array}{l} -p'(\phi)h'(c)[F_1 - F_2]\tilde{\nabla}\phi \\ +[1 - p(\phi)]h''(c)[F_1 - F_2]\tilde{\nabla}c \\ +[1 - p(\phi)]h'(c)[F'_1 - F'_2] \frac{1}{\xi} \tilde{\nabla} |\tilde{\nabla}\theta| \end{array} \right\}$$

The model is next applied to the case of eutectic solidification in a homogeneously undercooled Ag-Cu alloy, where the two solid phases have an fcc structure. The parameters $L_A = 1,097 \text{ J/cm}^3$, $T_A = 1,234 \text{ K}$, $L_B = 1,728 \text{ J/cm}^3$, and $T_B = 1,358 \text{ K}$ apply. The interaction parameters have been chosen so that the model phase diagram agrees qualitatively with the experimental one [$\Omega_L v = (16,000 - 4T)$

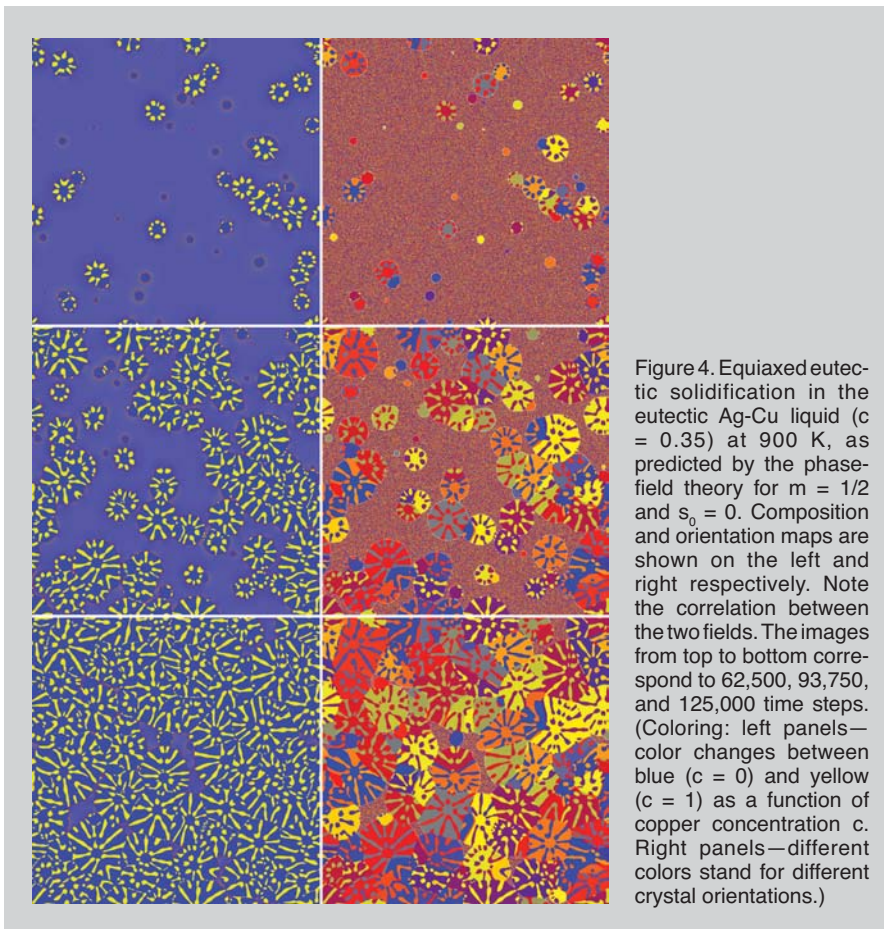


Figure 4. Equiaxed eutectic solidification in the eutectic Ag-Cu liquid ($c = 0.35$) at 900 K, as predicted by the phase-field theory for $m = 1/2$ and $s_0 = 0$. Composition and orientation maps are shown on the left and right respectively. Note the correlation between the two fields. The images from top to bottom correspond to 62,500, 93,750, and 125,000 time steps. (Coloring: left panels—color changes between blue ($c = 0$) and yellow ($c = 1$) as a function of copper concentration c . Right panels—different colors stand for different crystal orientations.)

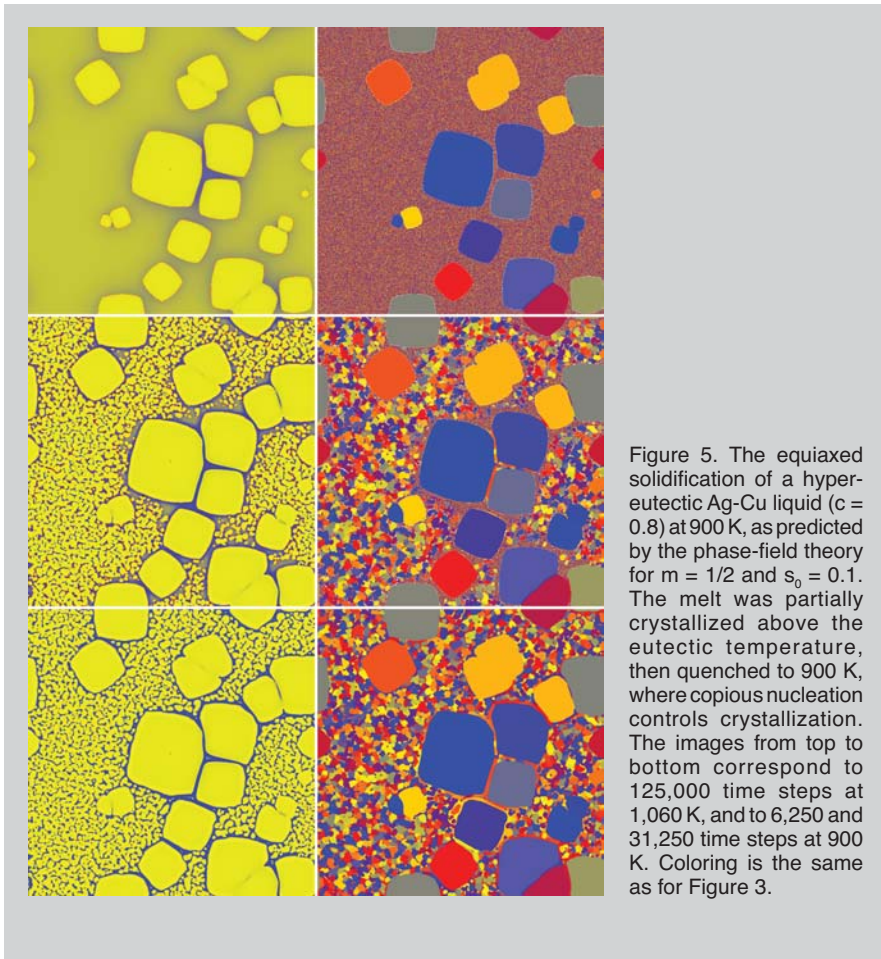


Figure 5. The equiaxed solidification of a hypereutectic Ag-Cu liquid ($c = 0.8$) at 900 K, as predicted by the phase-field theory for $m = 1/2$ and $s_0 = 0.1$. The melt was partially crystallized above the eutectic temperature, then quenched to 900 K, where copious nucleation controls crystallization. The images from top to bottom correspond to 125,000 time steps at 1,060 K, and to 6,250 and 31,250 time steps at 900 K. Coloring is the same as for Figure 3.

J/mol ; $\Omega_s v = (26,000 - 4T) J/\text{mol}$; $v = 8.7 \text{ cm}^3/\text{mol}$. At $T = 900 \text{ K}$, the equilibrium solid concentrations are $c_\alpha \approx 0.1$, and $c_\beta \approx 0.9$, while the eutectic concentration is 0.35. Assume that the diffusion in the solid is about 100 times slower than in the liquid and the orientation mobility is 10^5 times larger in the liquid than in the solid. The absolute size of the growth morphology is decreased by reducing the interface free energy by a factor of 6. The dimensionless time and spatial steps used are $\Delta \tilde{t} = 2.5 \times 10^{-7}$ and $\Delta \tilde{x} = 5 \times 10^{-3}$, while $\xi = 6 \times 10^{-6} \text{ cm}$. The simulations were performed on a $1,000 \times 1,000$ grid. With an appropriate choice of the parameters $a = 0.9/d$, $b = 0.1/d$, $m = 1/2$, $\psi = 0$, $d = \Delta \tilde{x}$, $\zeta_c = 1$, $\zeta_\theta = (\epsilon_\theta / \epsilon_\phi)^2$ (a relatively sharp orientation change is allowed at the interface), multigrain eutectic solidification is simulated. Note that the choice $m = 1/2$ gives preference to a step of $\Delta\theta = \pm 0.5$ in the orientation field at the $\alpha - \beta$ interface. Consequently, a particle of the dominant phase of orientation θ would prefer contact with a grain of the secondary crystalline phase of orientation $\theta' = \theta + \Delta\theta$ (i.e., in this

special case only a single relative orientation of the secondary phase is preferred). For $1 \geq m > 1/2$, two symmetric relative orientations appear ($\theta' = \theta \pm \Delta\theta$). The solidification morphologies obtained at two compositions [eutectic and hypereutectic ($c = 0.8$)] are shown in Figures 4 and 5. The model will be used to study equiaxed eutectic solidification and eutectic grain coarsening coupled to chemical diffusion.

CONCLUSION

Synthesizing of two methods described in this article will allow for greater flexibility in modeling of multi-phase, polycrystalline materials. Using the multi-phase-field method, each phase boundary energy can be controlled independently, leading to more realistic models for eutectic solidification.

ACKNOWLEDGEMENTS

Part of this work has been supported by contracts OTKAT037323, ESA Prodex 14613/00/NL/SFe, and ESA MAP Project No. AO99101.

References

1. K.A. Jackson and J.D. Hunt, *Transactions of the Metallurgical Society of AIME*, 236 (August 1966), pp. 1129–1142.
2. A. Karma, *Physical Review E*, 49 (1994), pp. 2245–2250.
3. K.R. Elder, J.D. Gunton, and M. Grant, *Physical Review E*, 54 (1996), pp. 6476–6484.
4. I. Steinbach et al., *Physica D*, 94 (3) (1996), pp. 135–147.
5. A.A. Wheeler, G.B. McFadden, and W.J. Boettinger, *Proceedings of the Royal Society of London, Series A Mathematical, Physical and Engineering Sciences*, volume 452 (London: Royal Society of London, 1996), pp. 495–525.
6. M. SeeBelberg and J. Tiaden, *Modeling of Casting Welding and Advanced Solidification Processes VIII*, ed. B.G. Thomas and C. Beckermann (Warrendale, PA: TMS, 1998), pp. 557–564.
7. B. Nestler and A.A. Wheeler, *Physica D*, 138 (2000), pp. 114–133.
8. F. Drolet et al., *Physical Review E*, 61 (2000), pp. 6705–720.
9. B. Nestler et al., *J. Crystal Growth*, 237 (2002), pp. 154–158.
10. J.A. Warren et al., unpublished.
11. W.J. Boettinger et al., *Annual Reviews of Materials Research*, 32 (2002), pp. 163–194.
12. W.J. Boettinger and James A. Warren, *Met. Trans. A*, 27A (1996), pp. 657–669.
13. J.W. Cahn and J.E. Hilliard, *Journal of Chemical Physics*, 28 (1) (1958), pp. 258–267.
14. S.M. Allen and J.W. Cahn, *Acta Metallurgica*, 27 (1979), pp. 1085–1095.
15. B. Nestler, *Physica D*, 141 (2000), pp. 133–154.
16. O. Penrose and P.C. Fife, *Physica D*, 43 (1) (1990), pp. 44–62.
17. R. Trivedi et al., *Metallurgical Transactions A*, 22 (10) (1991), pp. 2523–2533.
18. Y.L. Lin et al., *Metallurgical Transactions A*, 7 (1976), pp. 1435–1441.
19. L. Gránásy, T. Börzsönyi, and T. Pusztai, *Physical Review Letters*, 88 (art. no. 206105–1–4) (2002).
20. L. Gránásy, T. Börzsönyi, and T. Pusztai, *J. Crystal Growth*, 237–239 (2002), pp. 1813–1817.
21. L. Gránásy et al., *Nature Materials* 2 (2) (2003), pp. 92–96.
22. R. Kobayashi, J.A. Warren, and W.C. Carter, *Physica D*, 140 (2000), pp. 141–150.
23. W.C. Swope and H.C. Andersen, *Physical Review B*, 41 (1990), pp. 7042–7054.
24. P.R. ten Wolde, M.J. Ruiz-Montero, and D. Frenkel, *Physical Review Letters*, 75 (1995), pp. 2714–2717.
25. U. Gasser et al., *Science*, 292 (5515) (2001), pp. 258–262.
26. J.A. Warren and W.J. Boettinger, *Acta Metallurgica et Materialia*, 43 (1995), pp. 689–703.
27. R. Kobayashi, J.A. Warren, and W.C. Carter, *Physica D*, 119 (34) (1998), pp. 415–423.

Daniel Lewis, James Warren, and William Boettinger are with the Metallurgy Division of the National Institute of Standards and Technology in Gaithersburg, Maryland. Tamás Pusztai and László Gránásy are with the Research Institute for Solid State Physics and Optics in Budapest, Hungary. (Daniel Lewis is currently with General Electric Co. in Niskayuna, NY.)

For more information, contact Daniel Lewis, General Electric Co., Ceramic and Metallurgy Technologies, Building MB223, One Research Circle, Niskayuna, NY 12309; (518) 387-4538; fax (518) 387-5576; e-mail lewis@research.ge.com.